Ann. Geophysicae 14, 941–960 (1996) © EGS – Springer-Verlag 1996

Annales Geophysicae

Simulating the global atmospheric response to aircraft water vapour emissions and contrails: a first approach using a GCM

M. Ponater, S. Brinkop, R. Sausen, U. Schumann

DLR, Institut für Physik der Atmosphäre, Oberpfaffenhofen, D-82234 Weßling, Germany

Received: 6 September 1995/Revised: 4 March 1996/Accepted 26 March 1996

Abstract. The effect of contrails and aircraft water vapour emissions on global climate is studied by means of a general circulation model (GCM). In a first approach water vapour emissions and mean contrail coverage within the main flight routes are prescribed according to current observations in a simplified manner. A hierarchic experiment strategy with gradual increase of the forcing is applied to identify the resulting climate signals. The water vapour increase to be expected from air traffic is too small to force a detectable radiative or climatic response. The sensitivity of the model climate to the occurrence of contrails appears to be higher. For mid-latitude summer conditions, the high cloud increase experiments show a consistent temperature response pattern. However, its magnitude is statistically significant only for a mean contrail coverage exceeding present-day amounts. Moreover, the magnitude of the contrail climate signal is highly sensitive to the details of the experimental setup due to several non-linearities of the cloud-radiative interaction. Hence, the prescription of contrails in the GCM has to be as careful as possible for an optimal treatment of the problem. Respective recommendations are given.

1 Introduction

During the 1970s and early 1980s potential environmental impacts of aircraft emissions were studied in some detail, in particular concerning changes in the chemical composition of the atmosphere due to supersonic traffic (e.g. Johnston, 1971; CIAP, 1975). Since that time worldwide subsonic air traffic has increased significantly (by about 6% per year in the period 1978–1988, according to Nüsser and Schmitt, 1990), and this development can be expected to continue. Hence, interest in aircraft emissions to the atmosphere has grown anew, as the potential of a significant impact on the climate system has become conceivable (e.g. Held, 1988; Johnson *et al.*, 1992; Schumann, 1994; WMO, 1995).

Aircraft emissions may force the atmosphere in several different ways: radiatively active gases and aerosols may either be directly emitted or may be produced from the emissions by subsequent chemical reactions. Additional high clouds (contrails) may be triggered by water vapour and other emission components. One of the major direct emissions is carbon dioxide (CO_2). However, due to the long atmospheric residence time of CO_2, there is no need for a separate treatment of its aircraft-related part, as this effect is included in conventional global warming studies (e.g. Stouffer *et al.*, 1989; Cubasch *et al.*, 1992). Of particular interest is the emission of nitrogen oxides (NO_x), which have an impact on the atmospheric ozone chemistry. The dispersion and the chemical effect of NO_x from aircraft emissions have been studied quite recently by a number of authors (see Schumann, 1995, and references therein).

In the present study we focus on the direct radiative impact of water vapour emissions and their indirect effect via contrails. These questions have so far been treated mainly on the basis of principle considerations (Grassl, 1990; Liou *et al.*, 1990; Schumann and Wendling, 1990) or by means of one-dimensional (1D) models (e.g. Fortuin *et al.*, 1995; Strauss, 1995). However, no answer has been given to the question of whether the local radiative forcing and subsequent dynamical feedbacks may result in a significant large-scale response. Three-dimensional (3D) global general circulation models (GCMs) offer a suitable tool to approach this problem. We have made use of the atmospheric GCM ECHAM (*ECMWF* model, *Ham*burg version) to conduct several series of experiments so as to provide the basis for a quantitative assessment of the specific climate impact of contrail formation and aircraft-related water vapour increase.

The ECHAM model incorporates all large-scale dynamical feedback mechanisms that are relevant for the response to the radiative input caused by changes in water

Correspondence to: M. Ponater

vapour or high clouds. It must be borne in mind, however, that clouds are one of the most crucial components in GCMs, as the whole range of microphysics has to be parametrized for grid boxes of considerable size. Moreover, the possibilities of checking the validity of the respective parametrizations are limited. There is a definite lack of observations concerning cloud water content, ice particle size, and also water vapour content at aircraft cruising altitudes. As discussed by Stephens and Tsay (1990) and recently recalled by Cess *et al.* (1995) even our current theoretical understanding of solar radiation absorption by clouds does not appear to be comprehensive.

A further difficulty in giving reliable estimates of the large-scale impact of aircraft emissions arises from the smallness of the additional water vapour forcing. A significant increase of the atmospheric water vapour mixing ratio by aircraft emissions may occur in the lower stratosphere, where the residence time of the emissions is expected to be between 2 and 6 months (Schumann, 1994; Menzies and Tratt, 1995). Contrails, on the other hand, do not form mainly from aircraft-emitted water vapour. Water vapour from the environment is extensively included in the condensation process, as additional condensation nuclei become available due to emission of soot, sulphur components, etc.. In regions affected by main flight routes, the contrail coverage can be very large on individual days. Nevertheless, as far as observations are available for longer time periods, the amount of contrail coverage reaches (at most) 2% on long-term average (e.g. Bakan *et al.*, 1994). Except for a few regions, this is well below the range of natural variability for high cloud coverage simulated by the GCM. Hence, we have to apply an appropriate strategy that uses both statistical significance and physical consistency in order to establish a well-defined response of the atmosphere to the aircraft-related forcing.

The model and the experiment strategy are described in Sect. 2. The design of the water vapour sensitivity experiments and their results are presented in Sect. 3, while Sect. 4 deals in a similar way with the contrail sensitivity experiments. Section 5 includes a discussion of the results in the context of previous investigations. Some recommendations for further research work concerning the subject are formulated. Finally, Sect. 6 summarizes the conclusions and includes a brief outlook.

2 Model description and experiment strategy

2.1 The ECHAM model

The ECHAM GCM has been developed to be used for a wide range of climate sensitivity simulations. Successful applications include, for example, studies of the climate impact arising from changes in aerosol concentration (Bakan *et al.*, 1991; Graf *et al.*, 1993) and from the anthropogenic increase of greenhouse gases (Cubasch *et al.*, 1992; Lunkeit *et al.*, 1996). Tracer transport simulations were also performed, in particular with respect to the dispersion of aircraft NO_x-emissions (Sausen and Köhler, 1994).

ECHAM is a 3D spectral model, which uses vorticity, divergence, temperature, (logarithm of) surface pressure, water vapour mixing ratio, and cloud water mixing ratio as prognostic variables. It contains parametrization schemes for radiation, convection, cloud processes and precipitation, vertical and horizontal diffusion, and land surface processes. A comprehensive description of various versions of ECHAM, including a comparison and validation of their respective basic climatologies, is given by Roeckner *et al.* (1992). In the present study we restrict the model description to those features that are of particular relevance to the problem addressed.

We have chosen an upgraded version of the operational ECHAM3 GCM (Roeckner *et al.*, 1992; Lohmann and Roeckner, 1995). In this specific model version water vapour and cloud water are advected according to a semi-Lagrangian scheme (Rasch and Williamson, 1990) in the grid point domain, avoiding the occurrence of negative mixing ratios, which are frequently produced by the standard spectral advection scheme. The experiments were performed in T21 spectral horizontal resolution, i.e. the equivalent spatial resolution for dynamical processes is approximately 1000 km. The associated Gaussian transform grid, on which non-linear and diabatic terms (and the semi-Lagrangian advection scheme) are calculated, has a resolution of approximately 5.6°. The vertical resolution is characterized by 19 layers using a hybrid σ-p coordinate system, the model top being located at 10 hPa. The time step is 2400 s in a semi-implicit scheme. All experiments discussed in the present work were run in perpetual-January and perpetual-July mode, respectively, i.e. the insolation was fixed to mid-January or mid-July conditions. However, the diurnal cycle of solar irradiance was always included. The sea surface temperature was prescribed according to climatological values for the respective months.

From anthropogenic greenhouse gas increase experiments it is known that interactive clouds and water vapour are most important feedback mechanisms that modify the direct ("dry") response considerably. However, as demonstrated by Cess *et al.* (1990), a much higher degree of model-dependency is found with respect to the strength of the cloud feedback than with respect to the clear-sky response. Hence, the details of the parametrization schemes for clouds and cloud-radiative interaction are of particular interest for the response experiments presented here.

In ECHAM3, the prognostic tracers water vapour and cloud water are felt by the radiation scheme described by Hense *et al.* (1982). Cloud emissivity and optical thickness are calculated from the cloud water content according to Stephens (1978). Single scattering albedo and backscattering coefficients are used as given by Hense *et al.* (1982) and Kerschgens *et al.* (1978). The cloud scheme has been derived from ideas of Sundqvist (1978). According to the fractional cloud cover b each grid box is divided into a cloud-covered part and a cloud-free part. All cloud water in a given grid box is attributed to the cloud-covered part. The treatment of condensation, evaporation, precipitation, and sedimentation of ice crystals is described in detail by Roeckner *et al.* (1992). A diagnostic

partition of cloud water into liquid and ice component is made as a function of temperature (Rockel *et al.*, 1991). The fractional cloud cover is derived from the relative humidity r through the relationship

$$b = \begin{cases} \dfrac{r - r_0}{1 - r_0}, & r \geq r_0 \\ 0, & r < r_0 \end{cases} \quad (1)$$

where r_0 is a prescribed threshold value of relative humidity. This kind of critical parameter is used by many cloud parametrization schemes, although with differences in details (e.g. Walcek, 1994, his Fig. 1). In ECHAM3, r_0 is specified (at upper levels and in the presence of stable stratification) to be 85%. Grid boxes with a mean humidity below r_0 remain cloud-free, while overcast conditions are reached for $r = 100\%$. If grid boxes containing clouds are located at adjacent layers within one column, it is assumed that maximum overlap occurs for the cloudy parts of these boxes. Otherwise random overlap is assumed.

2.2 *The experimental strategy*

Within the model framework just described, the response arising from local water vapour emissions and enhanced high cloud coverage was determined. All experiments reported hereafter were extended over 18 months simulation time in the perpetual-January or -July mode, respectively. For each case, we conducted a control run with the standard model and a number of sensitivity simulations where certain parameters were changed with respect to control state. Long-term means were calculated from the last 15 month's data of each run, neglecting the first 3 months to be independent of the initial conditions and to assure a quasi-stationary behaviour of each experiment. The equilibrium response of any sensitivity experiment with respect to the control run was analysed in terms of the differences between the respective long-term monthly means. These differences should not be misinterpreted as arising in a mechanistic way from the parameter changes that characterize the sensitivity experiment. We must regard them as a net response, where the primary influence of the parameter change is superimposed by a multitude of feedbacks included in the model and taking part in the cause-and-effect relationship. Feedbacks from the ocean surface do not occur, as an uncoupled atmospheric GCM is used. Hence, the development of the temperature response is to some extent restricted. We account for this by considering (in addition to the temperature response) the radiative response at the top of the atmosphere as a measure of climate sensitivity.

Each of the time-averaged fields representing the climate mean state for some January or July experiment is associated with a well-defined range of internal (or natural) variability. Hence, the significance of any response can be checked with statistical tests. We chose the simple univariate t-test approach (e.g., Sachs, 1982) to test the null hypothesis of statistically identical long-term averages for a given significance level. The internal variability was estimated by the standard deviation of monthly means. It was assumed that the monthly means for a given quantity are Gaussian distributed and that they are statistically independent, if only every second month of a perpetual simulation is considered. Thus, the number of independent samples for each experiment was eight. These assumptions are certainly acceptable for the troposphere and the lower stratosphere. For some experiments, the stability of the response was checked with respect to the length of the integrations. With one exception discussed in Sect. 3.2, all signals classified as significant by the t-test proved to be stable. Thus, the 15 months analysed can be regarded as completely sufficient for the experiments discussed hereafter.

As mentioned in the introduction, a statistically significant signal is not likely to be forced by aircraft emissions arising under present-day conditions. However, the insignificance of some response in a statistical sense does not automatically indicate that the response is physically meaningless. To account for this possibility we conducted an experiment hierarchy, in which the strength of the forcing was gradually increased for both the water vapour and the contrail sensitivity problem. The idea is to establish a response, which is statistically significant for an artificially enhanced forcing, but which may also be attributed to weaker forcing conditions due to pattern consistency. This approach will prove successful, if the response turns out to be sufficiently linear.

3 Water vapour emission experiments

3.1 *Experimental design*

Besides CO_2, water vapour is the most abundant product in the exhaust of aircraft engines. An estimation of the 3D distribution of these emissions (Fig. 1) has been made available by the Warren Spring Laboratory (McInnes and Walker, 1992) on the basis of scheduled international and regional passenger and cargo flights for 1 month (September 1989). The corresponding globally integrated water vapour emission rate amounts to about 200 Mt/y. Transferred to the grid used by the ECHAM model, emission maxima may reach values of about 5×10^{-14} kg(H_2O)/(m^3 s) at cruising altitudes in the North Atlantic/North American region (Fig. 1, top), where the grid boxes have a volume of approximately 6×10^{14} m^3.

The emissions are given to the model as an additional source of water vapour, with no change from time step to time step. Like the background water vapour, the additional water is recognized by both the radiation scheme and the cloud scheme. Figure 2 demonstrates the magnitude of the background concentration for the upper troposphere and lower stratosphere, as simulated by ECHAM. Two characteristic mean profiles (averaged over the Northern Hemisphere extratropics north of 40° N) are given for January and July conditions, respectively. Values range from about 20 ppmv in the vicinity of the tropopause to between 2 and 5 ppmv for levels above 16 km. In the troposphere the concentration increases rapidly. These features are largely consistent with

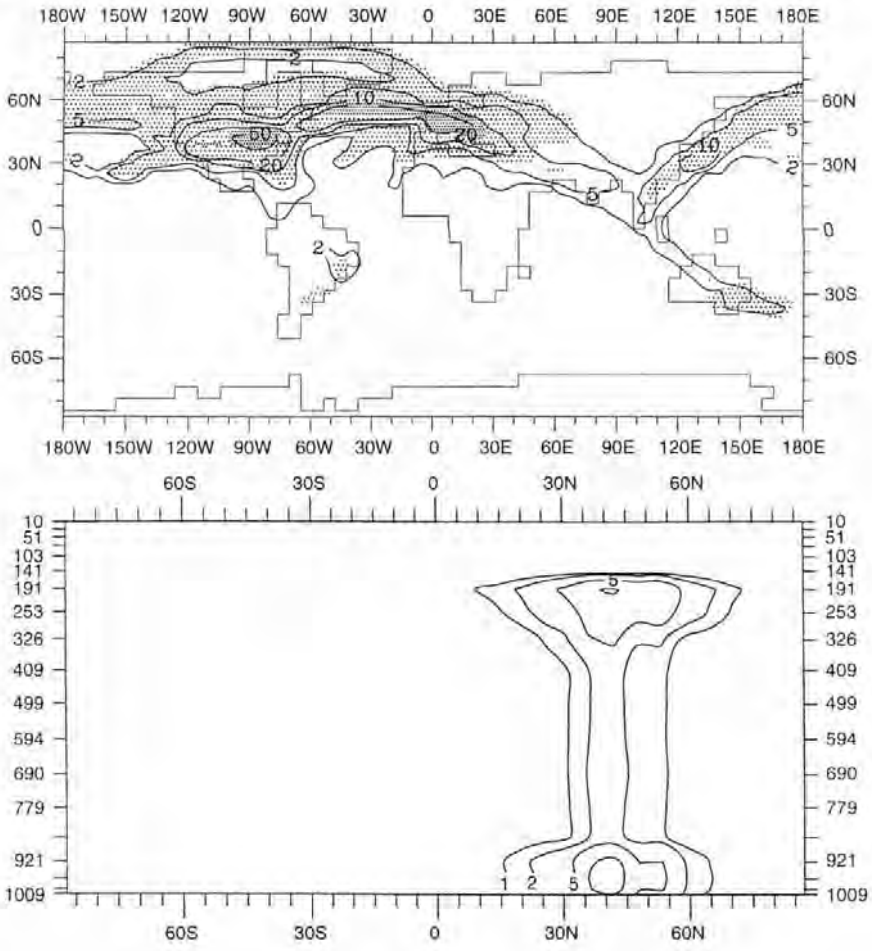

Fig. 1. Water vapour emission rates due to air traffic. *Top panel:* emission rates at model layer 7 (centred at about 190 hPa). *Bottom panel:* zonal mean cross section. Units are 10^{-15} kg/m^3 s. *Light (heavy) shading* in the *upper panel* indicates regions, where the emissions exceed the background concentration by 0.01‰ or by 0.1‰, respectively

observations, like those recently measured by Dessler *et al.* (1995). It is important to note that the aircraft-related increase of water vapour mixing ratio per time step (i.e. per 40 min) is four to five orders of magnitude smaller than the background mixing ratio at cruising altitudes (Fig. 1, top). Clearly, any climate response must depend on the atmosphere's ability to accumulate water vapour in the lower stratosphere. However, due to the low vertical model resolution (to be noted from the ordinate in the bottom panel of Fig. 1), all model layers affected by the aircraft emissions become part of the troposphere at least sometimes during the course of a long-term model integration. Gradual increase of water vapour mixing ratio on the time scale of months is thus unlikely to occur in the ECHAM model.

As explained in the preceding section, a hierarchy of experiments with systematically increasing forcing was created. Besides the basic sensitivity experiment using the original water vapour emission data set, the emission rates were enhanced by factors of 10, 100, 1000, and 10000, respectively, in four additional experiments. The enhancement was done only for model levels between 320 hPa and 150 hPa (i.e. in heights between about 9 and 13 km), where the majority of aircraft emissions are released (cf. Fig. 1, bottom). These are also the altitudes, where the largest climatic impact from a water vapour concentration increase can be expected (Grassl, 1990).

3.2 Results

The results of the water vapour emission sensitivity experiments were compared with the respective reference runs for perpetual-January as well as perpetual-July conditions. When the original emission data were used or when the respective values were increased by factors 10 or 100, no significant change of any relevant climate variable was identified. In particular, the cloud and temperature distribution and the radiative balance at the top of the atmosphere show no organized response whatsoever. This result is easy to understand from the magnitude considerations given, as no significant long-term trend of the upper level water vapour mixing ratio was noticed.

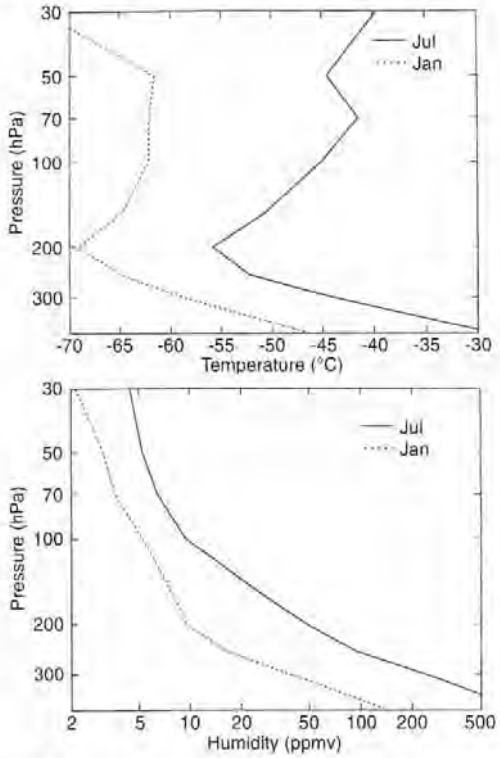

Fig. 2. Vertical profile of temperature (*top*) and water vapour mixing ratio (*bottom*) at levels between 400 hPa and 30 hPa. Averages over the Northern Hemisphere north of 40° N and over 15 months of an ECHAM control simulation are shown

The situation changes for the factor 1000 experiment. Here, the enforced water vapour increase is still much smaller than the background concentration, but it approaches the magnitude of the interannual standard variation (i.e. the natural variability) of water vapour in larger regions over North America and the North Atlantic near the 200-hPa level. This leads to a marked increase of cloudiness over the eastern United States, which is locally significant in a statistical sense. However, the response in the radiative balance and in the 3D temperature distribution remains weak, i.e. hardly significant on the large scale.

If we proceed further to the factor 10000 experiment, the water vapour emissions per time step have reached a magnitude in the range of the background concentration of water vapour in those geographical regions indicated by dark shading in Fig. 1 (top). The emissions exceed the natural variability in these regions, thus providing a highly significant increase in water vapour concentration. The resulting climate response is significant on the hemispheric scale. This is a consequence of extensive additional cloud formation at upper tropospheric layers, particularly over the continental areas of the Northern Hemisphere extratropics. The influence of the clouds to the radiative balance seems to be much stronger than that of the water vapour itself.

Table 1. July reference values of selected climate parameters (mean and interannual standard deviation) and their response to artificially enhanced (factor 10000) aircraft water vapour emissions. Averages over the area north of 30° N are shown. All response values are statistically significant on at least a 99% level

	Control	Response to H_2O-emissions
Top solar radiation (W/m^2)	301.9 ± 1.3	-4.4
Top thermal radiation (W/m^2)	-241.5 ± 0.9	$+5.6$
Top net radiation (W/m^2)	60.4 ± 1.2	$+1.2$
Total cloud cover (%)	51.1 ± 0.8	$+7.2$
Cloud water content (g/m^2)	83.6 ± 3.8	$+3.7$
Water vapour content (kg/m^2)	23.5 ± 0.5	$+1.5$

With respect to our main subject of determining the climatic impact of air traffic, the factor 10000 experiment is highly artificial. The enhancement of water vapour in the troposphere is much stronger than could ever occur in reality. Hence, we will not enter too deeply into a discussion of the results, but will use them as a qualitative example of the GCM response evolving in this kind of experiments. Table 1 gives the equilibrium response of some cloud and radiation parameters for the factor 10000 sensitivity experiment, compared with July reference conditions. Averages over the area north of 30° N are shown. The significant increase of cloud coverage, cloud water content and water vapour content is accompanied by a decrease of incoming shortwave radiation and a decrease of outgoing longwave radiation at the top of the atmosphere. Note that downward radiative fluxes are characterized by positive values. The radiative response is straightforward. The increase of mainly high clouds leads to an enhanced albedo and stronger backscattering in the solar part, so the climate system receives less energy. On the other hand, energy is gained as less thermal radiation is emitted to space by the (cold) clouds in the sensitivity experiment than by the (warm) Earth's surface in the control experiment (greenhouse effect of clouds). Both parts of the radiative response partly compensate, but in this case a significant net radiative energy gain of the system is produced. Figure 3 shows the resulting zonal mean atmospheric temperature change with a significant warming within the Northern Hemisphere troposphere and a cooling in the stratosphere. The warming is strongest immediately below those layers where the additional water vapour has been induced and where the additional clouds have formed. A zonal mean temperature increase of about 3 K is reached at 300 hPa and 50° N. Above the cloud layer considerable cooling of about 2 K occurs. For the respective January experiment we find a very similar response with respect to cloud cover and thermal radiation, but there is no significant increase of air temperature within the troposphere. Possible reasons for this remarkable difference will be discussed in Sect. 4.

In Fig. 3 considerable temperature differences can be noted in the stratosphere between 5° S and 65° S, which partly reach the 99% level of statistical significance. This response feature is, however, not robust but shows rather a random behaviour within the experiment hierarchy. The

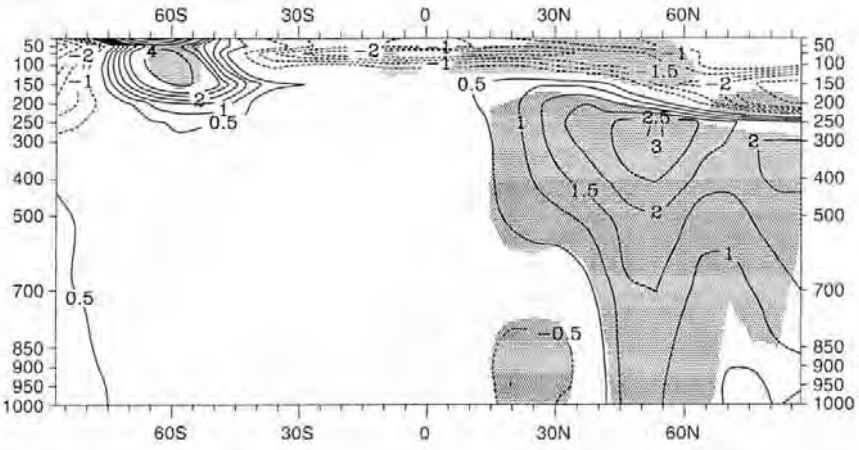

Fig. 3. July response of zonal mean temperature to artificially enhanced (factor 10000) water vapour emission rates from air traffic. Units are K. *Shading* indicates regions, for which the response passes the statistical significance test at the 99% level

reason is probably some spurious variability simulated by ECHAM in the vicinity of the polar night jet, as the latter is cut off at the model's upper boundary. We attribute no physical significance to this kind of remote response and will disregard the Southern Hemispheric stratosphere for the remainder of this study.

The main experience from the experiments described in this section is the absence of any detectable response due to water vapour increase alone. Even if enhanced by a factor of 100, the water vapour increase due to aircraft emissions remains too small compared to the respective natural variability. This appears to be consistent with similar numerical experiments by Rind and Lonergan (1995), concerning the climatic effect of stratospheric water vapour increase. In their results, a significant and robust response shows up only for a doubling of stratospheric water vapour concentration, a forcing too strong to be created by current air traffic.

In our experiments, the model climate responds as soon as a significant amount of clouds forms from the additionally induced water vapour. However, the factor 1000 and factor 10000 experiments discussed in this section cannot be regarded as a reasonable contrail sensitivity test. The source of additional water vapour available to force cloud formation is much too high compared to that actually provided by present-day aircraft emissions rates. In the real atmosphere, such extreme moistening is not needed since additional condensation would be triggered by emitted particles, a mechanism that is not accounted for in the experiments discussed above. In the following section we apply a more appropriate experiment setup to account for the potential climatic effect of contrails.

4 High cloud increase experiments

4.1 Experimental design

In regions strongly affected by air traffic, the fraction of the sky covered by contrails may reach local maxima of 6/8 and more under appropriate atmospheric background conditions. When averaged over longer time periods, however, the contribution of contrails to the total of high clouds is generally considered to be small. Contrail statistics on the hemispheric scale for multi-year periods are not available. From visual inspection of NOAA/AVHRR infrared satellite images of the East Atlantic/Western Europe area for a total of 7 years Bakan *et al.* (1994) estimated a contrail coverage of less than 1% along the North Atlantic flight corridor, with regional maxima of about 2% occurring for spring and summer conditions. These values are still somewhat higher than those previously given (Roll, 1990; Schumann and Wendling, 1990). As a guideline for the present study we will assume that under present-day conditions a value of 2% forms an upper limit for the time-mean contrail coverage over the regions associated with the main flight routes (see Fig. 1, top panel).

The following considerations may serve to outline the relative role of short-lived and persistent contrails for the mean observed contrail coverage. The area covered by contrails can be calculated as

$$A = N_A f_C L_C B_C. \tag{2}$$

where N_A is the number of aircraft en route, f_C is the fraction of aircraft generating contrails, and $L_C B_C$ measures the average width and length of contrails. The number of aircraft en route can be estimated from the global fuel consumption $M_F \approx 160$ Mt/y, the average fuel consumption per aircraft and time unit $m_F \approx 6.4$ kg/km for the present fleet of jet aircraft (Schumann, 1995), and an estimated average speed of each aircraft of $V \approx 800$ km/h, giving $N_A = M_F/(m_F V) \approx 3600$. Note that this average applies for constant traffic without daily or seasonal cycles, which is consistent with the time-independent cloud cover values used in our simulations.

Short-lived contrails occur when the ambient air temperature is cooler than some threshold value, which depends on the flight level, ambient humidity and aircraft propulsion efficiency. A typical value is -40 °C (Appleman, 1953; Busen and Schumann, 1995). According to Detwiler and Pratt (1984), who discussed the frequency of

Table 2. Area fraction of contrails estimated for present air traffic for short-lived and persistent contrails relative to the surface of the globe, the extratropics, and the flight route area

	Non-persistent contrails	Persistent contrails
Global	$1.3 \cdot 10^{-6}$	0.04%
Northern extratropics	$5.3 \cdot 10^{-6}$	0.18%
Routes	$17 \cdot 10^{-6}$	0.56%

contrail occurrence as well as their width and length on the basis of various observations over continental USA, aircraft spend 25% of their flight time under such conditions. They report that contrails are visible from a surface station, at least occasionally, on 32% of all days. In contrast, Schumann and Wendling (1990) found contrails in satellite pictures for an area of 300 000 km^2 in mid-Europe on 63% of all analysed satellite scenes.

When the humid air in the wake of the aircraft is mixed with dry ambient air to subsaturation with respect to ice, contrails swiftly evaporate. In the absence of precise information about the dependency of the width and length of short-lived contrails on external parameters like aircraft wing span, temperature, humidity, or turbulence, it appears reasonable to assume that short-lived contrails occur at less than $f_C = 0.63$ of all times with $B_C = 100$ m, $L_C = 3$ km. This yields $A_S = 680$ km^2 as an upper bound for their global coverage.

Persistent contrails form in air supersaturated with respect to the ice phase. Such regions typically occur ahead of cyclonic storms or downstream from convective cloud complexes, predominantly between the subtropical and polar jet streams. The width of the contrails depends on lateral mixing by turbulence and shear, while the lifetime is related to the time in which the ice particles generated in the contrail reach a size large enough to sediment out of the supersaturated layer (Detwiler and Pratt, 1984). During flights over continental USA, persistent contrails were observed 7% of the time when the flight was in clear or partly clouded regions. Surface observations revealed an average width of $B_C = 8.5$ km, and length of $L_C = 105$ km (Detwiler and Pratt, 1984). These data are roughly consistent with the satellite data reported. Hence, the global area coverage by persistent contrails may be of the order $A_P = 225\,000$ km^2.

In order to estimate the contrail coverage fraction, we relate these areas to either the surface of the globe (509×10^6 km^2), or the northern extratropics (127×10^6 km^2 north of 30°N), or the area of the main flight routes (about 40×10^6 km^2). This results in contrail cloud cover fractions as listed in Table 2.

Though the results from these highly simplified calculations may be uncertain by one order of magnitude, they show that short-lived contrails cover a very small area fraction. The computed fraction remains below 0.1% even when the number of aircraft flying is increased by about three orders of magnitude. However, the coverage of persistent contrails may not be negligible. The computed fraction in range of 1% in the traffic region is largely consistent with the satellite observations cited.

In order to transform all this information into a basis for systematic GCM experiments, the initial idea was to make use of the parametrization as given by Eq. (1): if more condensation nuclei are available, the chance for cloud formation increases and thus the threshold value r_0 should be somewhat lower for grid boxes frequently crossed by airplanes. From the aircraft emission data set we created a mask determining the locations, where aircraft H_2O emissions exceed a certain threshold value, so that contrails can be expected to occur most likely and most frequently there. At cruising altitudes in the so-defined area r_0 was decreased in the sensitivity experiments, intending to induce "contrails" (i.e. an increase of high cloud coverage) in the desired order of magnitude. However, the time-mean fractional cloud cover b proved to be rather insensitive to the value of r_0. It turned out that at the respective altitudes the model tends to simulate (on a time-step basis) conditions that are either very dry ($r < 30\%$) or very moist ($r \approx 100\%$). Thus, a marked increase of b could only be forced through an unreasonably strong reduction of r_0. Unfortunately, there is no global coverage of sufficiently reliable humidity measurements at altitudes above 300 hPa that would allow a decision to be made, whether the bimodal relative humidity distribution is a model artefact or not. Anyway, this kind of experiment failed to provide useful results concerning the climatic impact of contrails.

We therefore turned to an alternative approach, where the cloud thermodynamics would not be directly involved. In the areas covered by the "emission mask" explained already, the fractional cloud cover was enhanced by a constant increment only for the calculation of the solar and thermal radiative forcing. It was assumed that contrails possess the same optical properties as natural high clouds in the same grid box. This would be questionable for young contrails containing many small particles, but seems to be reasonable in a climate experiment, as the decisive contribution to the climatological mean contrail coverage comes from persistent contrails. Thus, we left the cloud water mixing ratio unchanged, except for those grid boxes containing no natural cirrus and, hence, no cloud water. In the latter case, a standard value had to be specified, as otherwise the "contrails" (i.e. the additional clouds) would not have been recognized by the radiation scheme. The standard value was chosen according to the climatological mean cloud water mixing ratio at the respective location. The original values of cloud cover and cloud water were retained for all other processes included in the ECHAM model. In choosing this procedure, we ensure that only the radiative forcing is directly modified by the additional high clouds. However, due to feedback mechanisms, the internal cloud coverage will also change. As will be shown below both increase and decrease of "natural cirrus" are possible. The sum of the natural high cloud change and the prescribed amount of contrails may be called the *effective* high cloud response. The effective cloud response eventually determines the equilibrium climate response and vice versa. A favourable feature of the constant-increment approach is the rather controlled way, in which the primary forcing is changed.

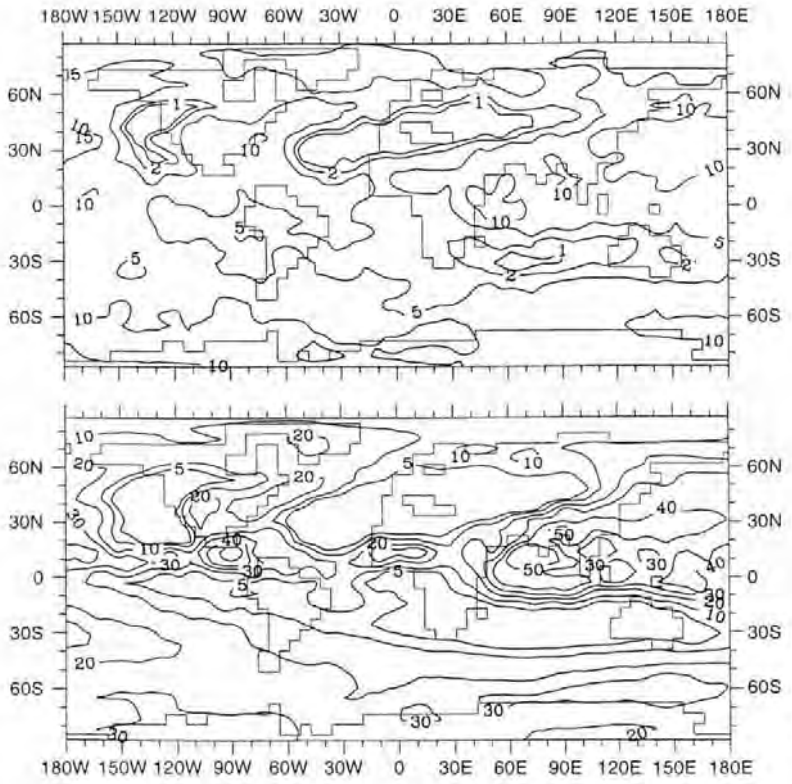

Fig. 4. Cloud coverage simulated by the ECHAM model at the 200 hPa level for July reference conditions. *Bottom panel* shows an average over 15 months of the control run, *top panel* shows the respective monthly mean standard deviation. Units are %

Following the experiment strategy outlined in Sect. 2, three basic experiments were performed, where the artificial increment imposed on the fractional cloud cover b was specified as 0.10, 0.05, and 0.02, respectively. Only levels between 150 hPa and 320 hPa (i.e. model layers 6 to 9) were affected. Additional sensitivity checks were made with respect to the influence of the standard value of cloud water mixing ratio assumed for grid boxes free of natural high clouds, and with respect to the number of model layers at which additional clouds were introduced. An appropriate selection from the results of these experiments is presented and discussed in the following subsections.

4.2 Equilibrium response for July conditions

As mentioned in Sect. 3, the temperature effect arising from high cloud changes appears to be larger for July than for January. Hence, we will first present the results of the July contrail experiments. Before discussing the response to the prescribed high cloud increase we present the background distribution of cirrus cloud coverage and the respective internal (climatic) variability. The bottom panel of Fig. 4 shows the global long-term mean cloud distribution at the 200 hPa level as simulated in the perpetual-July reference experiment. A comparison with cirrus observations from ISCCP data given by Hartmann *et al.* (1992) indicates satisfactory agreement. The largest cirrus coverage is, of course, found in the tropics along the innertropical convergency zone and in the Indian monsoon region. This area is only slightly affected by aircraft emissions (compare with Fig. 1). Along the main flight routes over the North Atlantic and near the east coast of Asia moderate cirrus cloudiness of 20–30% can be noticed. In contrast, the sub-tropical high pressure regions associated with large-scale sinking motion stand out as nearly cloud-free ($b < 0.05$). In the southern part of Europe these regions overlap the domain of strong air traffic. For this particular area not only the climatological mean cloudiness but also the interannual standard deviation (Fig. 4, top) is quite small. Hence, we may expect that a fixed prescribed contribution of contrails will leave a significant impact more easily here than elsewhere within the Northern Hemisphere extratropics.

As an example, the effective cloud response at 200 hPa is given in the top panel of Fig. 5 for the experiment, in which an increase of cloud coverage by 0.05 has been prescribed at four model levels between 150 hPa and 320 hPa. The bottom panel shows the corresponding response of the internal high clouds. In Fig. 5, top, the pattern of the main flight routes can clearly be recognized, which indicates a dominance of the prescribed change of cloud coverage over the secondary response arising from internal feedbacks. Outside the regions with heavy air traffic a general decrease of cloudiness is evident. The shading in Fig. 5, top, indicates that only over the eastern North Atlantic and Europe the cloud response is strong enough to pass the local t-test at the 99% significance

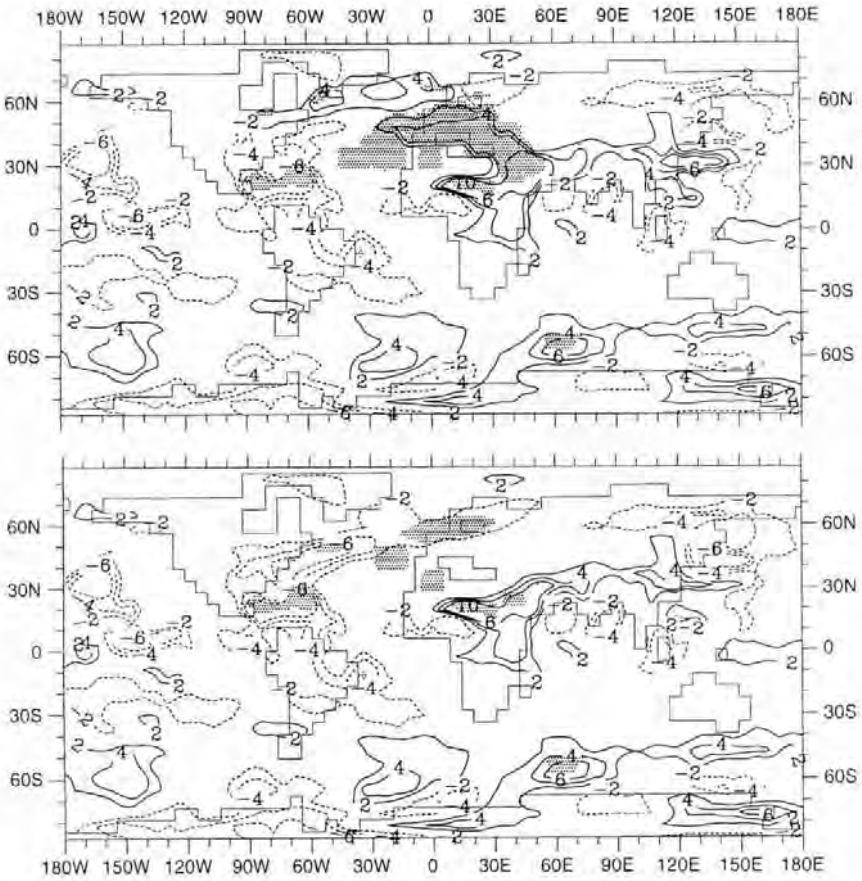

Fig. 5. July response of natural high cloud coverage (*bottom panel*) and effective high cloud coverage (*top panel*) at the 200 hPa level to a prescribed local enhancement of clouds by 0.05 (see text). Units are %. *Shading* indicates regions, where the response passes the statistical significance test at the 99% level

level. As expected, the highest t-values appear over southern Europe. In contrast, nearly all remote changes in the Southern Hemisphere and within the tropics, and also the response around the flight routes over East Asia are classified as locally insignificant. While the difference patterns remain similar at the other altitudes affected by the prescribed contrails, the statistical significance of the response gradually decreases with height as natural cloud coverage and its variability both increase (not shown). The t-values associated with the effective cloud response are, of course, higher in the experiment where the cloud increment due to air traffic is prescribed as 0.10. In the experiment where the enhancement is only 0.02, the effective response of cloud coverage at 200 hPa is significant only over small localized areas.

The radiative response at the top of the atmosphere is presented in Fig. 6 (thermal radiation) and Fig. 7 (solar radiation) for the $+0.05$ and $+0.10$ experiments, respectively. The main features of the response are confined to those locations where the clouds have changed, with hardly any (significant) changes elsewhere. As already explained, the response within the longwave spectral range describes the energy gain (positive values in Fig. 6) of the atmosphere/surface system due to the cloud greenhouse effect. The shape of the response pattern is quite similar in both experiments, while peak values amount to about 35 W/m^2 in the $+0.05$ experiment and to about 50 W/m^2 in the $+0.10$ experiment. The largest increase is found in the Middle East region. In fact, the main flight regions are most suggestively reproduced, particularly in the top panel of Fig. 6. The similarity between both sensitivity experiments is less distinct for the shortwave radiative response (Fig. 7), which represents the energy loss of the system due to an increased albedo. In the $+0.10$ experiment the albedo effect is strong with values up to -60 W/m^2 over the Middle East. The familiar structure of the main flight routes is again evident. However, in the $+0.05$ experiment the response pattern is more diffuse and significant changes occur only in the Mediterranean and Middle East region. Evidently, the shortwave radiative response at the top of the atmosphere increases non-linearly with increasing high cloud coverage.

This non-linearity is even more apparent in Table 3, where spatial averages of the radiative and effective cloud response are summarized. The absolute values from the reference experiment and the response to the three different increments of high cloud coverage increase are given for the solar, thermal, and net radiative balance at the top of the atmosphere, as well as for the atmospheric part of the system. Spatial averages have been calculated for the

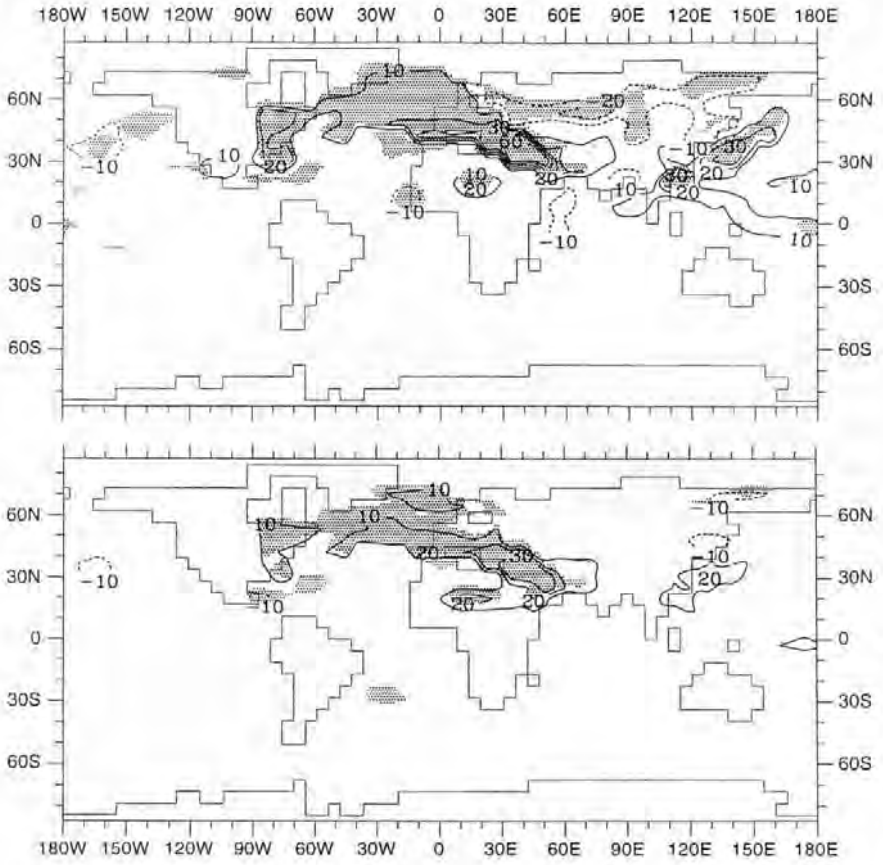

Fig. 6. July response of the thermal radiation balance at the top of the atmosphere to a prescribed local enhancement of high clouds by 0.10 (*top panel*) or by 0.05 (*bottom panel*). Units are W/m^2. *Shading* indicates regions, where the response passes the statistical significance test at the 99% level

whole globe, for the Northern Hemisphere extratropics (i.e. the area north of 30°N), and for that part of the Northern Hemisphere that is directly affected by main flight routes. The signals were replaced by an asterisk, if they did not pass a *t*-test at the 99% level.

Only few significant changes occur for globally averaged parameters, a result which is not surprising if one considers the distinctly localized character of the radiative forcing in Figs. 6 and 7. On the other hand, the +0.02 experiment does not produce much of a significant response either, even if averaging is restricted to the main flight routes. Evidently, the forcing is too weak in this experiment to produce a thorough impact that could generally match the level of internal variability. The most straightforward signal can be noticed for the radiation balance. The energy loss of the atmosphere/surface system due to thermal radiation (i.e. the outgoing thermal radiation at the top of the atmosphere) is strongest in the control experiment and decreases almost linearly as the amount of prescribed high clouds increases. The additional supply of longwave radiative energy in the sensitivity experiments is mainly absorbed by the atmospheric subsystem (noticed from the atmospheric thermal radiation balance response), while only a small portion is of benefit to the Earth's surface. The energy gain of the system by solar insolation is largest in the control experiment. In contrast to the thermal component, an extremely non-linear dependency of the shortwave energy balance on the additional high cloud coverage is apparent in the sensitivity experiments. Within the flight route regions a moderate decrease is found for the +0.02 and the +0.05 experiments, but a very sharp one for the +0.10 experiment. Only in the latter case is the shortwave energy supply significantly reduced on the hemispheric (and even global) average. The response of the net radiative balance at the top of the atmosphere changes its sign from the +0.05 experiment to the +0.10 experiment. In the former case, the cloud greenhouse effect dominates over the cloud albedo effect. The opposite is true for the +0.10 experiment. As the solar radiative input mainly affects the Earth's surface (while shortwave absorption by the atmosphere is small), we find a similar sign reversal for the surface net radiative balance as for the top of the atmosphere. In contrast, the dominance of the thermal radiative component for the atmospheric part of the climate system leads to a gradual increase of atmospheric net radiative heating with increasing forcing.

If the large-scale radiation balance changes by a magnitude as apparent from Figs. 6 and 7, and Table 3 (for a prescribed high cloud increment of 0.05 or 0.10), the

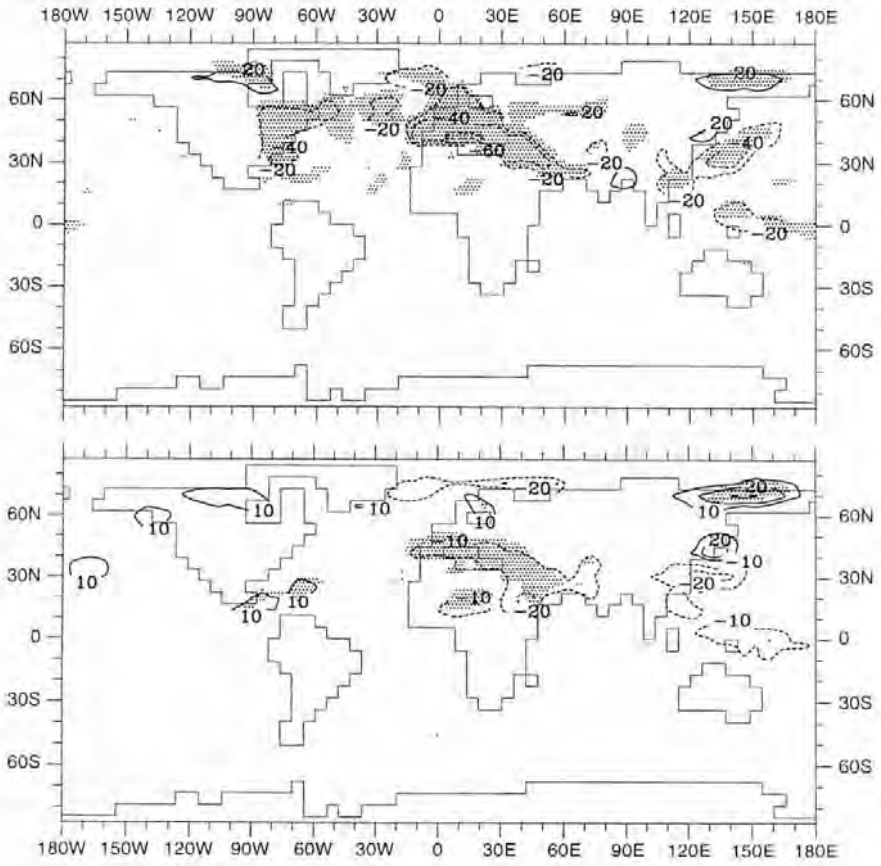

Fig. 7. As Fig. 6, but for the solar radiation balance at the top of the atmosphere

temperature distribution can be expected to change as well. However, feedback mechanisms with other processes than radiation may amplify or damp the primary disturbance. The resulting equilibrium response of the July zonal mean temperature is shown in Fig. 8 for all three increments. A consistent temperature signal is found in the Northern Hemisphere extratropics. The dominant feature is a general warming of the troposphere with its maximum at the layers where the effective high cloud coverage has increased. Secondary features of the signal are a cooling at layers above the additional clouds and another slight cooling in the lower troposphere at subtropical latitudes. It is noteworthy that this response pattern is quite similar to that of Fig. 3, where the clouds formed interactively from an excess of water vapour in the upper troposphere. Regarding the +0.10 experiment the temperature increase is significant over almost the whole extratropical troposphere above 500 hPa. A maximum of more than 4 K is reached at 55°N and at 200 hPa. Apart from a much weaker peak value of about 1.6 K warming, the response is similar in the +0.05 experiment. In the +0.02 experiment, the overall response is still similar in structure but its significant part is confined to a narrow latitudinal band and only few model layers.

Figure 9 gives a representative impression of the horizontal distribution of the temperature response at 200 hPa, using the +0.05 experiment as an example. While the cloud-radiative equilibrium response at this level has been shown to be largely confined to regions in the vicinity of the main flight routes, the temperature signal is spread over a larger area. Parts of the warmer air are evidently advected into remote regions. Nevertheless, the zonal asymmetry remains considerable. The temperature response shown in Fig. 9 is classified as 99% significant over almost the whole North Atlantic and Europe.

4.3 Sensitivity studies

So far results from the primary series of experiments have been presented, where contrails were prescribed at four model layers located in the vicinity of the tropopause (see Sect. 4.1). Observed information about the vertical extension of a field of contrails is hardly available. In particular, we do not know whether the uppermost layer, for which additional clouds were prescribed in the primary series, is really affected by contrails. Therefore, additional sensitivity experiments were performed, where the prescribed contrails were restricted to three model layers (between

Table 3. July response of selected variables due to a prescribed local increase of high cloud coverage at four model layers. Averages over the globe, the Northern Hemisphere extratropics, and over main flight routes are given. Response values indicating statistical significance on a level smaller than 99% are omitted

Averaging domain	Control experiment	Response to +0.10 increase	Response to +0.05 increase	Response to +0.02 increase
Top solar radiation (W/m^2)				
Global	233.6 ± 0.5	−2.3	*	*
Northern extratropics	301.9 ± 1.3	−5.1	*	*
Flight routes	320.4 ± 3.3	−33.1	−5.6	−6.9
Top thermal radiation (W/m^2)				
Global	−236.9 ± 0.5	+1.3	+0.7	*
Northern extratropics	−241.5 ± 0.9	+2.4	+1.8	*
Flight routes	−243.9 ± 2.2	+23.8	+14.6	+6.2
Top net radiation (W/m^2)				
Global	−3.4 ± 0.6	−1.0	*	*
Northern extratropics	60.4 ± 1.2	−2.7	+2.4	*
Flight routes	76.4 ± 2.2	−9.3	+9.1	*
Atmospheric solar radiation (W/m^2)				
Global	65.7 ± 0.2	*	*	*
Northern extratropics	93.1 ± 0.6	−1.8	−1.4	−1.2
Flight routes	97.5 ± 1.1	−4.3	−3.8	−3.7
Atmospheric thermal radiation (W/m^2)				
Global	−166.8 ± 0.6	*	*	*
Northern extratropics	−170.9 ± 1.1	+2.2	+2.1	+1.2
Flight routes	−177.3 ± 1.7	+18.7	+12.6	+5.7
Atmospheric net radiation (W/m^2)				
Global	−101.1 ± 0.5	*	*	*
Northern extratropics	−77.8 ± 1.1	*	*	*
Flight routes	−79.7 ± 2.0	+14.4	+8.8	+2.0
Total cloud coverage (effective) (%)				
Global	53.2 ± 0.4	*	*	*
Northern extratropics	51.1 ± 0.8	−2.2	−1.4	*
Flight routes	52.2 ± 1.3	+2.2	*	*

190 hPa and 320 hPa) or to two model layers (between 190 hPa and 250 hPa). This was done for both the +0.05 and the +0.10 experiment, but only results for the latter case are shown here. Both the optical thickness of the contrail layer and its top and bottom height are subject to change in this kind of sensitivity experiment. The first modification should affect more strongly the albedo effect, while the second one will be most important for the greenhouse effect (Ockert-Bell and Hartmann, 1992).

Table 4 shows that the area averaged radiative balance is rather sensitive to the number of layers involved. We will base our discussion on the results from the areas, where the contrails have been introduced (see Figs. 6 and 7), as the global and the Northern Hemisphere extratropics responses are largely determined by the changes occurring in those areas. The shortwave radiative loss and longwave radiative gain of the climate system due to enhanced high cloud coverage both decrease in magnitude as the number of contributing layers is lessened. Note that the shortwave response dominates over the longwave one, yielding a net radiative cooling relative to the control run for all +0.10 experiments. The net radiative response also gradually decreases with a decreasing number of contrail layers. The +0.05 experiments (not shown) behave accordingly in the sense that they show a gradually decreasing *warming* net radiative response. The sign reversal of the net radiative response that is found for the +0.05 and +0.10 basic experiments thus turns out to be independent of the number of layers associated with the contrails.

The atmospheric subsystem exhibits a positive response of the radiative balance, which strongly decreases with the number of effective contrail layers, because the longwave radiative warming by the contrails decreases in mangitude while the shortwave cooling shows a non-monotonous behaviour. As the radiative forcing decreases with the number of layers involved, so does the temperature response. Figure 10 shows the respective signal arising from a cloud coverage increase by 0.10 at three layers. In comparison to Fig. 8 the atmospheric temperature increase is thoroughly reduced all over the Northern Hemisphere troposphere, while the pattern with maximum warming at the contrail level and immediately below is retained. The maximum warming of about 1.5 K at 200 hPa is still statistically significant at the 99% level. A similar result is gained from the +0.05 experiments.

In a second series of experiments we analysed the sensitivity of the basic experiment signals to the standard value that was specified for the cloud water mixing ratio of contrails in grid boxes without natural cirrus clouds. The experiments were conducted for additional high cloud increments of 0.10 or 0.05, respectively, at all four levels, but with only half of the standard values used in the basic

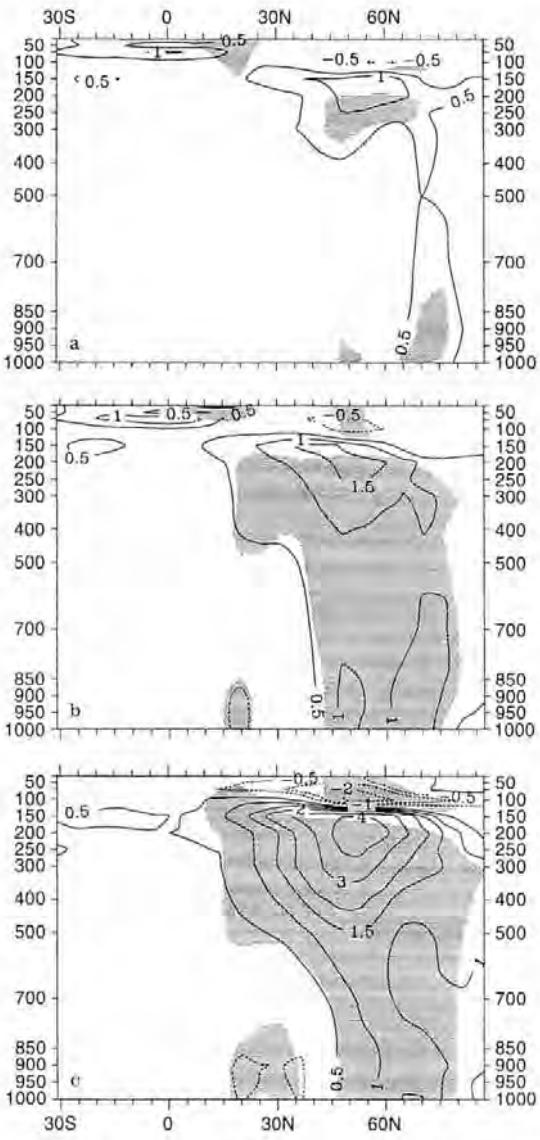

Fig. 8a–c. July response of zonal mean temperature to a prescribed local enhancement of high clouds at four upper levels (see text). Panels **a**, **b**, and **c** refer to increments of 0.02, 0.05, and 0.10, respectively. Units are K. *Shaded areas* indicate a response passing the statistical significance test at the 99% level

experiments. Thus, in these complementary experiments the "contrails" will be, on average, optically thinner than in the basic experiments. Table 5 and Fig. 11 display the respective response. Again the non-linearity of both the shortwave and the net radiative response is apparent. At the top of the atmosphere there is even an increase of the net response as the shortwave cooling due to the clouds dominates more strongly over the longwave warming when the optical thickness is reduced. For the atmospheric subsystem the cloud-induced shortwave absorption does not show much of a change while the longwave warming decreases. The strength of the temperature response decreases for the thinner contrails in the sensitivity experiments. We present the +0.10 case as a representative example (Fig. 11). A comparison with Fig. 8 and 10 suggests that the sensitivity of the temperature response to the number of layers associated with contrails is considerably stronger than the sensitivity to the specified value of contrail cloud water mixing ratio. The sensitivity of the radiative response is, however, not so different in both cases.

4.4 Equilibrium response for January conditions

Another perhaps even more surprising, example to emphasize that the relation between the radiative response and the temperature response is not necessarily straightforward are the results arising from the perpetual-January experiments. Table 6 shows the radiative response from experiments that have been performed in analogy to the basic July experiments presented in Table 3.

In January, the incoming solar radiation at the top of the atmosphere is much smaller than in July when averaged over the Northern Hemisphere extratropics. The solar radiative response to high cloud enhancement operates on a considerably lower level for the local winter season. The main difference between January and July responses is, thus, that the January radiative response is dominated by the thermal component not only for the atmosphere but also for the whole climate system. The net response at the top of the atmosphere is positive in all experiments, but (similar to the July results) its increase with increasing forcing is not linear. The radiative response for the atmospheric part of the system is only slightly different for January and July. Solar absorption plays hardly any role in January and the thermal and net radiative energy gain of the atmosphere indicate a rather linear increase with increasing high cloud coverage.

The atmospheric temperature response in January is generally positive for the Northern Hemisphere, but the temperature rise is so small that it remains insignificant in a statistical sense for all experiments. Hence, there is no sense in presenting any respective figure. The weakly developed temperature signal forms the fundamental deviation from the July results, particularly in view of the similarity of the radiative response. We will make an attempt to explain the relation between the radiative response and the temperature response in the next subsection.

4.5 The development of the temperature response

The various components of the atmospheric heating balance, which eventually determine the atmospheric equilibrium temperature, all change in the cloud sensitivity experiments relative to the control experiment. The radiative heating rates are directly forced by the prescribed cloud modifications. This primary forcing is modified by atmospheric feedbacks due to advection,

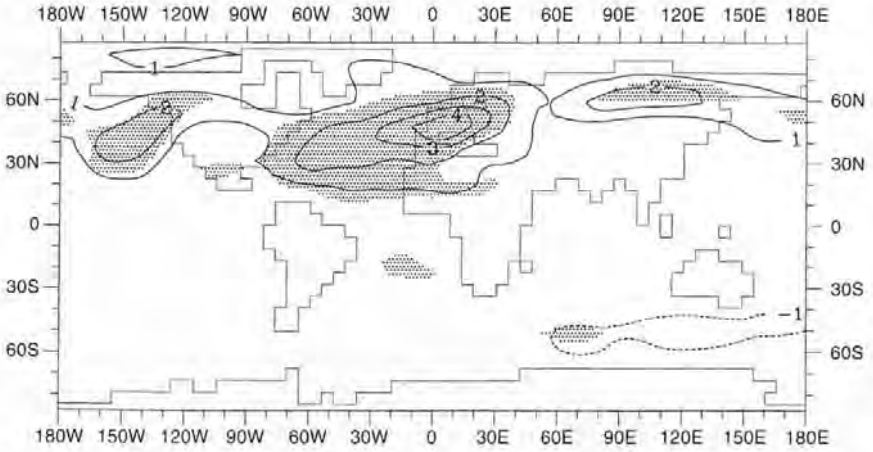

Fig. 9. July response of the 200 hPa temperature to a prescribed local enhancement of high clouds by 0.05. Units are K. *Shading* indicates regions, where the response passes the statistical significance test at the 99% level

Table 4. July response of selected variables due to a prescribed local increase of high cloud coverage by 0.10 at two, three, or four model layers. Averages over the globe, the Northern Hemisphere extratropics, and over the main flight routes are given. Signals that do not pass a *t*-test at the 99% level are omitted

Averaging domain	Control experiment	Response to +0.10 at 4 levels	Response to +0.10 at 3 levels	Response to +0.10 at 2 levels
Top solar radiation (W/m^2)				
Global	233.6 ± 0.5	−2.3	−1.3	−1.4
Northern extratropics	301.9 ± 1.3	−5.1	−4.8	−3.7
Flight routes	320.4 ± 3.3	−33.1	−25.4	−18.5
Top thermal radiation (W/m^2)				
Global	−236.9 ± 0.5	+1.3	+1.2	+1.1
Northern extratropics	−241.5 ± 0.9	+2.4	+3.2	+2.6
Flight routes	−243.9 ± 2.2	+23.8	+19.4	+15.2
Top net radiation (W/m^2)				
Global	−3.4 ± 0.6	−1.0	*	*
Northern extratropics	60.4 ± 1.2	−2.7	−1.6	−1.1
Flight routes	76.4 ± 2.2	−9.3	−6.0	−3.3
Atmospheric solar radiation (W/m^2)				
Global	65.7 ± 0.2	*	−0.6	−0.3
Northern extratropics	93.1 ± 0.6	−1.8	−2.0	−1.7
Flight routes	97.5 ± 1.1	−4.3	−8.0	−6.7
Atmospheric thermal radiation (W/m^2)				
Global	−166.8 ± 0.6	*	+1.3	*
Northern extratropics	−170.9 ± 1.1	+2.2	+3.1	+1.5
Flight routes	−177.3 ± 1.7	+18.7	+17.5	+12.5
Atmospheric net radiation (W/m^2)				
Global	−101.1 ± 0.5	*	+0.7	*
Northern extratropics	−77.8 ± 1.1	*	+1.1	*
Flight routes	−79.7 ± 2.0	+14.4	+9.5	+5.8

convection, condensation etc. Hence, it is not sufficient to look at the changes in the total or atmospheric radiation balance. All physical processes affecting the heat balance have to be considered, in order to understand how the temperature response in the contrail experiments actually develops.

In the following we discuss vertical profiles of area averaged heating rates caused by the various physical processes. This method has been frequently applied to explain the temperature response in GCM experiments. For example, Lohmann and Roeckner (1995) used it to demonstrate the sensitivity of the tropical circulation to the parametrization of cloud emissivity in ECHAM. Here we focus on the Northern Hemisphere extratropics, where practically the whole forcing and response from air traffic occurs. According to the mask described in Sect. 4.1 we separate the area north of 30°N into that part directly affected by the prescribed contrails and the remaining part, in which the response is basically indirect. The time-averaged heating rates do not differ significantly for these

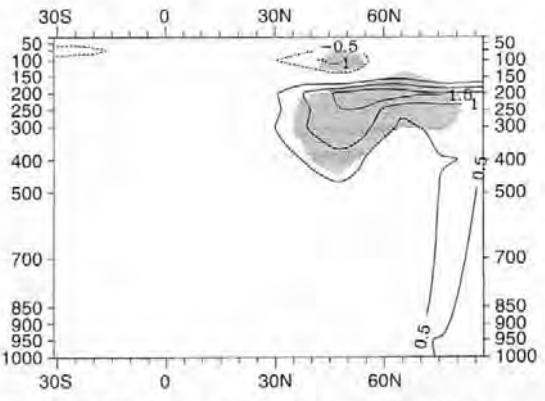

Fig. 10. As Fig. 8c, but for a local enhancement of high clouds by 0.10 at three upper levels

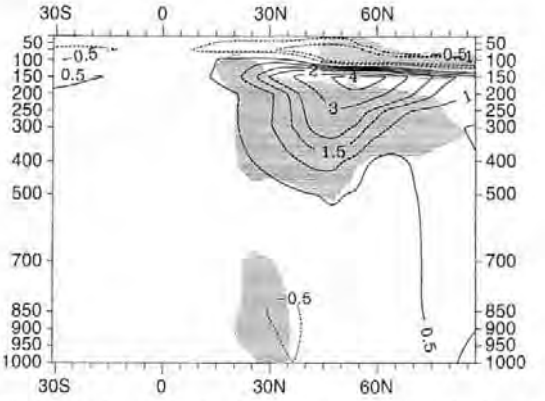

Fig. 11. As Fig. 8c, but for the experiment, in which the cloud water content of contrails was halved with respect to the standard sensitivity experiment (see text)

two sub-domains, hence a discussion of the characteristic features for the area associated with the contrails (Fig. 12, left panel) is sufficient. The profiles are taken from the July reference experiment. The radiative balance of the atmosphere is negative, as the longwave cooling dominates the warming by solar absorption. The resulting net radiative cooling is balanced by the other processes, mainly by condensation and convection, vertical diffusion, and, above the boundary layer, by adiabatic warming. As the 15-month means displayed in Fig. 12 represent a quasi-stationary state, the total heating rate is close to zero. The shaded bands around the curves indicate the monthly mean standard deviation in the control experiment, i.e. the internal variability of the heating rates. It is small enough to allow an interpretation of the response behaviour in the sensitivity experiments.

The changes of the heating rates arising from the additional high cloud increment of 0.10 at four layers are displayed in Fig. 12, right panel. Again these profiles

Table 5. July response arising from a prescribed local high cloud coverage increase by 0.10 at four model levels as simulated for different values of the cloud water content prescribed in grid boxes without natural cirrus. Averages over the globe, the Northern Hemisphere extratropics, and over the main flight routes are given. Response values that do not pass a *t*-test at the 99% level are omitted

Averaging domain	Control experiment	Response to +0.10 increase (climatic cloud water)	Response to +0.10 increase (half climatic cloud water)
Top solar radiation (W/m^2)			
Global	233.6 ± 0.5	-2.3	-2.0
Northern extratropics	301.9 ± 1.3	-5.2	-6.2
Flight routes	320.4 ± 3.3	-33.1	-29.9
Top thermal radiation (W/m^2)			
Global	-236.9 ± 0.5	$+1.3$	$+1.0$
Northern extratropics	-241.5 ± 0.9	$+2.3$	$+2.5$
Flight routes	-243.9 ± 2.2	$+23.8$	$+18.2$
Top net radiation (W/m^2)			
Global	-3.4 ± 0.6	-1.0	-1.1
Northern extratropics	60.4 ± 1.2	-2.7	-3.7
Flight routes	76.4 ± 2.2	-9.3	-11.8
Atmospheric solar radiation (W/m^2)			
Global	65.7 ± 0.2	*	*
Northern extratropics	93.1 ± 0.6	-1.8	-1.5
Flight routes	97.5 ± 1.1	-4.3	-5.0
Atmospheric thermal radiation (W/m^2)			
Global	-166.8 ± 0.6	*	*
Northern extratropics	-170.9 ± 1.1	$+2.2$	$+1.7$
Flight routes	-177.3 ± 1.7	$+18.7$	$+15.5$
Atmospheric net radiation (W/m^2)			
Global	-101.1 ± 0.5	*	*
Northern extratropics	-77.8 ± 1.1	*	*
Flight routes	-79.7 ± 2.0	$+14.4$	$+10.5$

Table 6. January response of selected variables due to a prescribed local increase of cloud coverage. Averages over the globe, the Northern Hemisphere extratropics, and over main flight routes are given. Response values that do not pass a *t*-test at the 99% level are omitted

Averaging domain	Control experiment	Response to + 0.10 increase	Response to + 0.05 increase	Response to + 0.02 increase
Top solar radiation (W/m^2)				
Global	243.0 ± 0.8	*	*	*
Northern extratropics	54.4 ± 0.5	− 1.9	*	*
Flight routes	88.4 ± 0.8	− 9.4	− 2.6	− 2.6
Top thermal radiation (W/m^2)				
Global	− 227.6 ± 0.6	+ 1.3	*	*
Northern extratropics	− 189.9 ± 0.6	+ 4.2	+ 3.1	+ 0.7
Flight routes	− 205.6 ± 1.6	+ 20.0	+ 12.9	+ 5.5
Top net radiation (W/m^2)				
Global	15.4 ± 0.5	*	*	*
Northern extratropics	− 135.5 ± 0.4	+ 2.3	+ 2.7	*
Flight routes	− 117.2 ± 1.2	+ 10.6	+ 10.3	+ 2.9
Atmospheric solar radiation (W/m^2)				
Global	72.5 ± 0.2	*	*	*
Northern extratropics	28.8 ± 0.2	*	*	*
Flight routes	40.1 ± 0.4	− 2.0	*	*
Atmospheric thermal radiation (W/m^2)				
Global	− 166.8 ± 0.5	*	*	*
Northern extratropics	− 147.1 ± 1.1	+ 2.5	+ 2.7	*
Flight routes	− 144.2 ± 2.3	+ 16.0	+ 10.7	+ 4.2
Atmospheric net radiation (W/m^2)				
Global	− 94.2 ± 0.6	*	*	*
Northern extratropics	− 118.3 ± 1.0	+ 2.2	+ 2.6	*
Flight routes	− 104.1 ± 2.2	+ 14.0	+ 10.1	*

represent the regions directly influenced by the prescribed contrails, where significant changes of almost all components to the net heating rate occur. At the layers directly affected by the contrails the heating by solar absorption is increased. In this particular experiment the solar response is rather large, peaking at about 1 K/d for the uppermost cloud layer and dominating the longwave cooling response there. At about 300 hPa both radiative components warm the atmosphere. Below the contrail layer, in the middle and lower troposphere, a reduced longwave radiative cooling is associated with contrails. For most of the layers, this warming response outweighs the energy loss arising from less solar absorption in the contrail sensitivity experiment. The changes in the atmospheric radiative balance (consider also Table 3 for the vertically integrated atmospheric radiative heating rates in this experiment) are compensated mainly by adiabatic processes. Outside the flight-route regions (profiles are not shown here) we find an energy gain of the atmosphere by dynamical processes (most likely advection from the contrail regions), which is balanced by increased longwave radiative cooling arising from an enhanced mean temperature (e.g. as in Fig. 9). In both sub-domains the heating rate response related to convection and large-scale condensation remains small, while vertical diffusion plays a role only at the lowest levels.

The equilibrium states of the +0.10 and the control experiment compared in Fig. 2 (right) are both characterized by nearly vanishing total heating rates. Thus, we are still not able to draw a definite conclusion about the origin of the temperature rise in the contrail sensitivity experiment. Some insight can be provided by calculating differences between the heating rates of the "first months" of the two experiments (Fig. 13, left). Both experiments start from identical initial conditions, but the sensitivity experiment develops in a non-stationary way, because the atmosphere is adjusting to its new forcing. The resulting response profiles indicate which processes determine the total heating rate during the adjustment time. The comparison of two single monthly means will not produce results that are as statistically stable as the results of a comparison of two long-range means. Nevertheless, considering the small magnitude of the month-to-month variability of the area averaged heating rates (Fig. 12, left) at least a qualitative estimate can be gained.

If one compares the equilibrium heating rate response (Fig. 12, right) and the respective response for the first months (Fig. 13, left) there seem to be little differences at the first glance. However, as during the adjustment time of the sensitivity experiment the radiative warming response dominates over the adiabatic cooling at the levels of contrail occurrence, the net heating rate is of similar magnitude as the individual heating components. Evidently, at upper levels the atmosphere needs some time to create a modified circulation and a new balance between the various processes. Meanwhile, the temperature rises resulting in the response shown in Fig. 8.

For January conditions, the situation is different (Fig. 13, right); the warming by solar absorption is much weaker than in July. At the layers near the tropopause

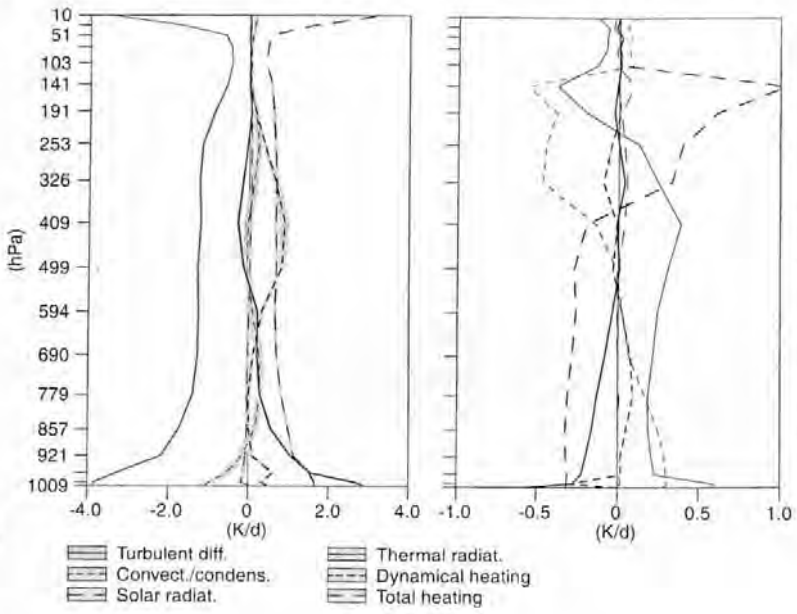

Fig. 12. Vertical profiles of various components of the heat budget equation, averaged over those regions north of 30° N associated with main flight routes. Time averages over the 15 months of the July reference experiment are shown, *shaded bands* indicate the monthly mean standard deviation (*left panel*). The *right panel* shows the equilibrium response of the heating rates to a prescribed local enhancement of high clouds by 0.10 at four upper levels. Units are K/d. Note that the *abscissa* is *scaled differently* in both panels

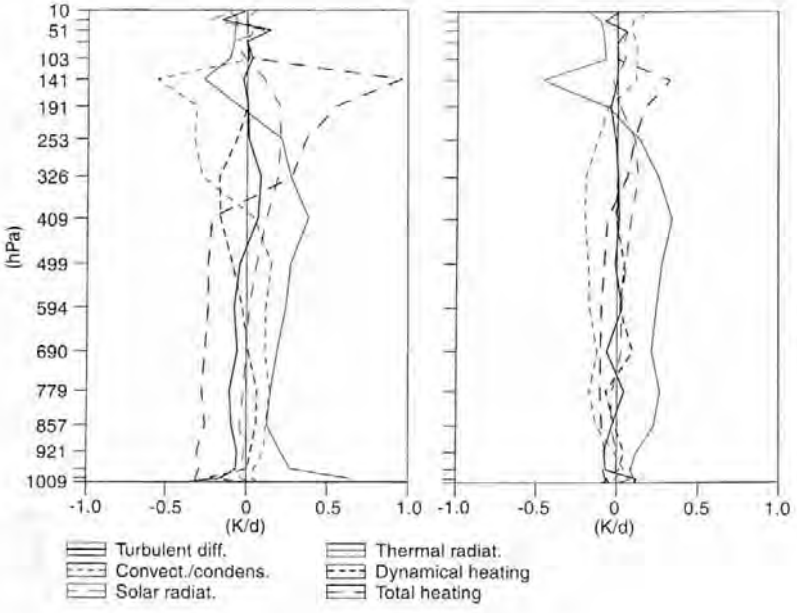

Fig. 13. Left panel is equivalent to Fig. 12 (*right*), but shows the response associated with the adjustment time of the high cloud increase experiment (see text). *Right panel* shows the respective response of the heating rates during the adjustment time of the corresponding January high cloud sensitivity experiment

(and above) no large radiative imbalance occurs that would require an equally large adiabatic compensation. For the troposphere, it appears that the longwave radiative warming due to the contrails is rather easily compensated by adiabatic effects within the vigorous wintertime atmospheric circulation. There is no need to rise the upper level temperature to a considerably higher level to achieve a new heat balance. Thus, it is mainly the constructive interference of solar and thermal heating at particular levels (around the tropopause) in July that causes the July and January temperature response to be qualitatively different.

5 Discussion

Results from two GCM experiment hierarchies with respect to the climatic impact of either aircraft water vapour

emissions or contrails have been presented. We can summarize the following five points as the main outcome. A climatic effect from air traffic is more likely to occur due to contrail formation than due to the accumulation of water vapour at levels around the tropopause. With air traffic restricted to the current main flight routes, contrails have to cover (on time average) about 5% of the sky to force a climate response that is statistically significant within the model framework. Backscattering and absorption of shortwave radiation depend in a highly non-linear fashion on coverage and optical thickness of the prescribed contrails. The radiative impact of the high cloud increase forces a unique atmospheric temperature response pattern under July conditions, while the temperature change is smaller and insignificant for January. The July response pattern contains a warming at tropospheric mid-latitudes, which is largest within the contrail layers, and which gradually decreases with height.

In a (somewhat simplified) attempt to generalize the results it may be stated that a significant climate response is to be expected within the model framework only if the water vapour or contrail forcing exceeds the internal monthly mean variability of background water vapour or cirrus clouds. Taking into account the magnitude considerations of Schumann (1994, his Table 3) and the comparison between emissions and background concentration presented in Fig. 1 it is thus not surprising that there is no response to the water vapour emissions. Even if the GCM could reflect accumulated stratospheric water vapour over a residence time of several months, horizontal mixing would most likely prevent the aircraft water vapour from reaching values in the range of the background water vapour in the lowermost stratosphere. Consider, for example, the net radiative forcing near the tropopause estimated by Fortuin *et al.* (1995) as a result of stratospheric water vapour increase due to air traffic. In that study, a residence time of 2.5 years (i.e. considerably longer than the 7 months given by Menzies and Tratt, 1995, as an upper limit) was assumed. The resulting concentration increase of water vapour was introduced to a 1D radiative convective model. The associated radiative response of about 0.1 W/m^2 would still remain too small to create a significant effect in the ECHAM GCM with its much larger variability of internal radiative forcing as shown in Tables 3 and 6. Therefore, we conclude that the water vapour increase due to air traffic is too small to force a 3D climate impact, which could be separated from the background variability in the framework of the current generation of circulation models.

Contrails, on the other hand, have been shown to carry the potential for a detectable large-scale climatic effect. We succeeded in establishing a characteristic signal that occurs even with a forcing close to present-day conditions, though it is not statistically significant in this latter case. Hence, the usefulness of the hierarchic experiment strategy has become apparent. The structure of the July temperature signal turned out to be quite robust throughout the experiments, suggesting a fair degree of reliability. Using the possibility to consider the complete atmospheric heat balance for particular areas, we were able to offer a physically consistent explanation for the qualitative difference of the January and July temperature response. The combination of shortwave and longwave absorption at the contrail layers provides a stronger local radiative heating for July. The local circulation change to restore the heat balance by enhanced adiabatic cooling has to be more substantial than in January, when shortwave radiative heating is of minor importance.

The magnitude of the July temperature signal proved to be strongly dependent on the details of the experimental design. The highly non-linear dependence of solar backscattering and solar absorption from cloud coverage, optical thickness, and cloud top height is of particular relevance. The simulated dominance of the albedo effect of high clouds over their greenhouse effect is not inconsistent with observations for optical thick clouds and high zenith angles (Hartmann *et al.*, 1992). On the other hand, the dominance of local solar atmospheric heating over the longwave cooling in some of our experiments (e.g. Fig. 13) does not fit with current observational evidence (see Ackerman *et al.*, 1988; or more recently Francis *et al.*, 1994). Probably, the optical thickness of our contrails is too high. One possible reason is the inadequate capture of ice cloud optical properties by the Stephens (1978) relation (Rockel *et al.*, 1991). Other reasons may be too many overlapping contrail layers, or an overestimated standard cloud water mixing ratio for the layers above 200 hPa, where the climatological mean value is based on a rather small number of natural cirrus formation events. The effect of the spatial inhomogeneity of the additional clouds has also not been included here, though it may be quite important (Harshvardhan and Randall, 1985), as inhomogeneous clouds possess an albedo lower than homogeneous ones with the same cloud water content. In any case, the prescription of a contrail coverage constant in space and time is not completely adequate to capture the non-linearities in the response mechanism. Finally, the effect of the solar response at the Earth's surface (non-linearly increasing with cloud coverage) has been completely neglected over ocean areas due to the use of an atmospheric GCM without an interactive ocean surface.

Hence, the magnitude of the temperature signals in Figs. 8–11 can only be regarded as a qualitative result at the present stage, most probably forming an upper limit to the actual effect of additional high clouds. There is, in particular, no much point in looking for a climatic response of higher order (i.e. with respect to baroclinicity, storm tracks, etc.) before the sensitivity of the temperature response to the use of a refined experiment strategy has been demonstrated. Such a strategy ought to give full account to the above-mentioned non-linearities of the forcing mechanism.

6 Conclusions

In this study a first approach to the simulation of the potential 3D climate response arising from aircraft water vapour emissions and contrails has been made. The radiative impact of water vapour concentration increase is too small to force a detectable large-scale climate signal. However, by using a hierarchic experiment strategy there is

a chance to detect a characteristic climate signal from contrails under mid-latitude summer conditions.

From the results of various sensitivity experiments it has become evident that the experimental setup has to be carried out extremely carefully to account for the non-linearities in the forcing arising from cloud-radiative interaction, particularly as the net climate response to be expected from air traffic will be small for a forcing close to present-day conditions. An upgraded experiment strategy should contain the application of a coupled atmosphere/mixed-layer ocean model to include feedbacks involving the sea surface temperature. It is also necessary to introduce a contrail parametrization that relates the occurrence of contrails to the local atmospheric state. In this way the potential of the GCM to solve the problem could be exploited in an optimal way.

There are a number of uncertainties with respect to the question, whether the optical properties of persistent contrails are different from those of natural cirrus clouds, particularly with respect to their optical thickness and to their particle size spectrum. Our current knowledge about these matters must be regarded as insufficient, thus subsequent GCM experiments could well profit from respective research progress. Finally, the effects of ozone chemistry modification and radiative effect of aircraft-related aerosols will have to be included to provide a complete simulation of the climatic effect of air-traffic.

Acknowledgements. The authors wish to express their thanks to a number of colleagues who supported this work by helpful discussions, namely Stefan Bakan, Andreas Chlond, Hans Feichter, Ulrike Lohmann, and Erich Roeckner (MPI für Meteorologie, Hamburg), Burkhardt Rockel (Forschungszentrum GKSS, Geesthacht), and Klaus Gierens (DLR, Oberpfaffenhofen). The aircraft emission data basic to the experiments were kindly provided by Michael Williams (WSL Lab.) and Alfons Schmitt (DLR, Köln). Thanks also to Christine Land for her assistance in analysing the model output. This work has received financial support by the BMBF within the project "Schadstoffe in der Luftfahrt".

Topical Editor L. Eynard thanks H. Grassl and another referee for their help in evaluating this paper.

References

Ackerman, T. P., K.-N. Liou, F. P. J. Valero, and L. Pfister, Heating rates in tropical anvils, *J. Atmos Sci.*, **45,** 1606–1623, 1988.

Appleman, H., The formation of exhaust condensation trails by jet aircraft, *Bull. Am. Meteorol. Soc.*, **34,** 14–20, 1953.

Bakan, S., A. Chlond, U. Cubasch, J. Feichter, H. Graf, H. Grassl, K. Hasselmann, I. Kirchner, M. Latif, E. Roeckner, R. Sausen, U. Schlese, D. Schriever, I. Schult, U. Schumann, F. Sielmann, and W. Welke, Climate response to smoke from burning oil wells in Kuwait, *Nature*, **351,** 367–371, 1991.

Bakan, S., M. Betancor, V. Gayler, and H. Grassl, Contrail frequency over Europe from NOAA-satellite images, *Ann. Geophysicae*, **12,** 962–968, 1994.

Busen, R., and U. Schumann, Visible contrail formation from fuels with different sulfur contents, *Geophys. Res. Lett.*, **22,** 1357–1360, 1995.

Cess, R. D., G. L. Potter, J. P. Blanchet, G. J. Boer, A. D. Del Genio, M. Deque, V. Dymnikov, V. Galin, W. L. Gates, S. J. Ghan, J. T. Kiehl, A. A. Lacis, H. Le Treut, Z.-X. Li, X.-Z. Liang, B. J. McAvaney, V. P. Maleshko, J. F. B. Mitchell, J.-J. Morcrette, D. A. Randall, L. Rikus, E. Roeckner, J. F. Royer, U. Schlese, D. A. Sheinin, A. Slingo, A. P. Sokolow, K. E. Taylor, W. M. Washington, R. T. Wetherald, I. Yanai, and M. H. Zhang, Intercomparison and interpretation of climate feedback processes in 19 atmospheric general circulation models, *J. Geophys. Res.*, **95,** 16601–16615, 1990.

Cess, R. D., M. H. Zhang, P. Minnis, L. Corsetti, E. G. Dutton, B. W. Forgan, D. P. Garber, W. L. Gates, J. J. Hack, E. F. Harrison, X. Jing, J. T. Kiehl, C. N. Long, J.-J. Morcrette, G. L. Potter, V. Ramanathan, B. Subasilar, C. H. Whitlock, D. F. Young, and Y. Zhou, Absorption of solar radiation by clouds: observations versus models, *Science*, **267,** 496–499, 1995.

CIAP, Final Report, US Department of Transportation, Climate Impact Assessment Program, DOT-TST-75-51–DOT-TST-75-58 (8 vols.), 1975.

Cubasch, U., K. Hasselmann, H. Höck, E. Maier-Reimer, U. Mikolajewicz, B. D. Santer, and R. Sausen, Time-dependent greenhouse warming computations with a coupled ocean-atmosphere model, *Clim. Dyn.*, **8,** 55–69, 1992.

Dessler, A. E., E. J. Hintsa, E. M. Weinstock, J. G. Anderson, and K. R. Chan, Mechanisms controlling water vapor in the lower stratosphere: a tale of two stratospheres, *J. Geophys. Res.*, **100,** 23167–23172, 1995.

Detwiler, A., and R. Pratt, Clear-air seeding: opportunities and strategies, *J. Weather Mod.*, **16,** 46–60, 1984.

Fortuin, J. P. F., R. van Dorland, W. M. F. Wauben, and H. Kelder, Greenhouse effects of aircraft emissions as calculated by a radiative transfer model, *Ann. Geophysicae*, **13,** 413–418, 1995.

Francis, P. N., A. Jones, R. W. Saunders, K. P. Shine, A. Slingo, and Zhian Sun, An observational and theoretical study of the radiative properties of cirrus: some results from ICE '89, *Q. J. R. Meteorol. Soc.*, **120,** 809–848, 1994.

Graf, H., I. Kirchner, A. Robock, and I. Schult, Pinatubo eruption winter climate effects: model versus observations, *Clim. Dyn.*, **9,** 81–93, 1993.

Grassl, H., Possible climate effects of contrails and additional water vapor, in: *Air-Traffic and the Environment*, Ed. U. Schumann, Lecture Notes in Engineering, **60,** Springer, Berlin Heidelberg New York, pp. 124–137, 1990.

Harshvardhan and D. A. Randall, Comments on "The parametrization of radiation for numerical weather prediction and climate models", *Mon. Weather Rev.*, **113,** 1832–1833, 1985.

Hartmann, D. L., M. E. Ockert-Bell, and M. L. Michelsen, The effect of cloud type on Earth's energy balance: global analysis, *J. Clim.*, **5,** 1281–1304, 1992.

Held, M. (Ed.), Ökologische Folgen des Flugverkehrs, *Tutzinger Materialien*, **50**/1989, ISSN 0930-1850, 1988.

Hense, A., M. Kerschgens, and E. Raschke, An economical method for computing radiative transfer in circulation models, *Q. J. R. Meteorol. Soc.*, **108,** 231–252, 1982.

Johnson, C. E. J. Henshaw, and G. McInnes, Impact of aircraft and surface emissions of nitrogen oxides on tropospheric ozone and global warming, *Nature*, **355,** 69–71, 1992.

Johnston, H. S., Reduction of stratospheric ozone by nitrogen oxide catalysts from supersonic transport exhaust, *Science*, **173,** 517–522, 1971.

Kerschgens, M., U. Pilz, and E. Raschke, A modified two-stream approximation for computations of the solar radiation budget in a cloudy atmosphere, *Tellus*, **30,** 429–435, 1978.

Liou, K. N., S. C. Ou, and G. Koenig, An investigation on the climatic effect of contrail cirrus, in: *Air-Traffic and the Environment*, Ed. U. Schumann, Lecture Notes in Engineering, **60,** Springer, Berlin Heidelberg New York, pp. 154–169, 1990.

Lohmann, U., and E. Roeckner, The influence of cirrus cloud-radiative forcing on climate and climate sensitivity in a general circulation model, *J. Geophys. Res.*, **100,** 16305–16323, 1995.

Lunkeit, F., R. Sausen, and J. M. Oberhuber, Climate simulations with the global coupled atmosphere-ocean model ECHAM2/OPYC, Part I: present-day climate and ENSO events, *Clim. Dyn.*, **12,** 195–212, 1996.

McInnes, G., and C. T. Walker, The global distribution of aircraft air polution emissions, *Warren Spring Lab., Rep.* **LR 872**(AP), 1992.

Menzies, R. T., and D. M. Tratt, Evidence of seasonally dependent stratosphere-troposphere exchange and purging of lower stratospheric aerosol from a multiyear lidar data set, *J. Geophys. Res.*, **100,** 3139–3148, 1995.

Nüsser, H. G., and A. Schmitt, The global distribution of air traffic at high altitudes, related fuel consumption and trends, in: *Air-Traffic and the Environment*, Ed. U. Schumann, Lecture Notes in Engineering, **60,** Springer, Berlin Heidelberg New York, pp. 1–11, 1990.

Ockert-Bell, M. E., and D. L. Hartmann, The effect of cloud type on Earth's energy balance: results for selected regions, *J. Clim.*, **5,** 1157–1171, 1992.

Rasch, P. J., and D. L. Williamson, On shape preserving interpolation and semi-Lagrangian transport, *SIAM J. Sci. Comput.*, **11,** 656–687, 1990.

Rind, D., and P. Lonergan, Modeled impacts of stratospheric ozone and water vapor perturbations with implications for high-speed civil transport aircraft, *J. Geophys. Res.*, **100,** 7381–7396, 1995.

Rockel, B., E. Raschke, and B. Weyres, A parametrization of broad band radiative transfer properties of water, ice and mixed clouds, *Beitr. Phys. Atmos.*, **64,** 1–12, 1991.

Roeckner, E., K. Arpe, L. Bengtsson, S. Brinkop, L. Dümenil, M. Esch, E. Kirk, F. Lunkeit, M. Ponater, B. Rockel, R. Sausen, U. Schlese, S. Schubert, and M. Windelband, Simulation of the present-day climate with the ECHAM model: impact of model physics and resolution, *Max-Planck-Institut für Meteorologie*, Rep. **93,** ISSN 0937-1060, 1992.

Roll, O., Kondensstreifen im Satellitenbild, *Diplomarbeit, Institut für Geophysik und Meteorologie*, University of Köln, Germany, 1990.

Sachs, L., Angewandte Statistik: anwendung statistischer Methoden, 6. Aufl., Springer, Berlin Heidelberg New York, 1982.

Sausen, R., and I. Köhler, Simulating the global transport of nitrogen oxides emissions from aircraft, *Ann. Geophysicae*, **12,** 394–402, 1994.

Schumann, U., On the effect of emissions from aircraft engines on the state of the atmosphere, *Ann. Geophysicae*, **12,** 365–384, 1994.

Schumann, U. (Ed.), AERONOX – The impact of NO_x emissions from aircraft upon the atmosphere at flight altitudes 8–15 km, EC-DLR publication on research related to aeronautics and environment, Oberpfaffenhofen, 1995.

Schumann, U., and P. Wendling, Determination of contrails from satellite data and observational results, in: *Air-Traffic and the Environment*, Ed. U. Schumann, Lecture Notes in Engineering, **60,** Springer, Berlin Heidelberg New York, pp. 138–153, 1990.

Stephens, G. L., Radiation profiles in extended water clouds. II: parametrization schemes, *J. Atmos. Sci.*, **35,** 2123–2132, 1978.

Stephens, G. L., and S.-C. Tsay, On the cloud absorption anomaly, *Q. J. R. Meteorol. Soc.*, **116,** 671–704, 1990.

Stouffer, R. J., S. Manabe, and K. Bryan, Interhemispheric asymmetry in climate response to gradual increase of atmospheric CO_2, *Nature*, **342,** 660–662, 1989.

Strauss, B., Über den Einfluß natürlicher und anthropogener Eiswolken auf das regionale Klima-mit besonderer Berücksichtigung des mikrophysikalischen Einflusses, *Diss.*, University of München, DLR-FB 94-23, ISSN 0939-2963, 1995.

Sundqvist, H., A parametrization scheme for non-convective condensation including prediction of cloud water content, *Q. J. R. Meteorol. Soc.*, **104,** 677–690, 1978.

Walcek, C. J., Cloud cover and its relationship to relative humidity during a springtime mid-latitude cyclone, *Mon. Weather Rev.*, **122,** 1021–1035, 1994.

World Meteorological Organisation, Scientific assessment of ozone depletion: 1994, *WMO, Global Ozone Research and Monitoring Project*, Rep. **37,** Geneva, 1995.